NUCLEAR
INSTRUMENTS
& METHODS
IN PHYSICS
RESEARCH
Section A

DISTO: a large acceptance multiparticle spectrometer for 1–3 GeV proton beams

F. Balestra[a], Y. Bedfer[b,1], R. Bertini[a,b,1], L.C. Bland[c,2], A. Brenschede[d,3,4],
F. Brochard[b,1], M.P. Bussa[a], V. Chalyshev[e,5], Seonho Choi[c,2], M. Debowski[f,g,6],
M. Dzemidzic[c,2], J.Cl. Faivre[b,1], I.V. Falomkin[e,5], L. Fava[a],
L. Ferrero[a], J. Foryciarz[f,h,6], V. Frolov[e,5], R. Garfagnini[a], D. Gill[i], A. Grasso[a],
E. Grosse[g,7], S. Heinz[b,1], W.W. Jacobs[c,2], W. Kühn[d,4], A. Maggiora[a],
M. Maggiora[a], A. Manara[a,b,1], D. Panzieri[a], H.W. Pfaff[d,4], G. Piragino[a],
G.B. Pontecorvo[e,5], A. Popov[e,5], J. Ritman[d,4], P. Salabura[f,6], P. Senger[g],
J. Stroth[j], F. Tosello[a], S.E. Vigdor*[c,2], B. Zalikhanov[e,5], G. Zosi[a]

[a]*Dipartimento di Fisica "A. Avogadro" and INFN, Torino, Italy*
[b]*Laboratoire National Saturne, CEA Saclay, France*
[c]*Indiana University Cyclotron Facility, Bloomington, IN, USA*
[d]*Physikalisches Institut, Univ. Gießen, Germany*
[e]*JINR, Dubna, Russia*
[f]*M. Smoluchowski Institute of Physics, Jagellonian University, Kraków, Poland*
[g]*GSI, Darmstadt, Germany*
[h]*H. Niewodniczanski Institute of Nuclear Physics, Kraków, Poland*
[i]*TRIUMF, Vancouver, Canada*
[j]*Institut für Kernphysik, Univ. Frankfurt, Frankfurt, Germany*

Received 15 September 1998

Abstract

A magnetic spectrometer system has been constructed for the study of reactions with multiple charged particles in the final state, induced by polarized proton beams of few GeV energy. The system is based on a large-gap dipole magnet, with

a liquid hydrogen target and scintillating fiber tracking detectors embedded inside the magnet. Multiwire proportional chambers, plastic scintillator hodoscopes, and threshold Cherenkov detectors placed outside the magnet provide additional tracking, triggering and particle identification capabilities. The system has been applied to study exclusive hyperon as well as pseudoscalar and vector meson production reactions at bombarding energies below 3 GeV. Additionally, it has been used to monitor the proton beam polarization at Laboratoire National Saturne. The components and performance of the system are reported. © 1999 Elsevier Science B.V. All rights reserved.

1. Introduction

The DISTO experiment was originally proposed [1] at Laboratoire National Saturne (LNS) in Saclay, France to probe the mechanism for the production of polarized hyperons in proton-induced reactions. A number of earlier experiments [2] at high bombarding energies had revealed sizable polarizations for Λ particles produced inclusively. The inclusive studies suffer from a serious ambiguity in distinguishing Λ's that are produced directly from those that result from the decay of heavier produced hyperons, such as the Σ^0. Thus, the goal of the DISTO collaboration was to provide kinematically complete measurements for a number of exclusive reaction channels, such as $pp \rightarrow pK^+\Lambda$ and $pp \rightarrow pK^+\Sigma^0$. For this purpose it is necessary to measure the momenta of the outgoing proton and kaon with sufficient resolution to distinguish Λ from Σ^0 production via their missing mass difference of 77 MeV. Furthermore, to determine the polarization of the outgoing Λ's, it is necessary to detect the proton and π^- that result from their weak decay (with a branching ratio of 64%) and to exploit the parity-violating asymmetry characteristic of this weak decay. The detection and vector momentum determination for these four charged products yields a kinematically complete measurement even for those reaction channels where a neutral decay daughter [e.g., γ in the case of the $\Sigma^0(1192)$ or π^0 for $\Sigma^0(1385)$] goes undetected.

In order to constrain the hyperon production mechanism, it is desirable for the apparatus to cover reactions over a large fraction of the available phase space. This is especially important for the Λ's decay phase space, if one is to achieve high sensitivity to the Λ polarization, with minimal instrumental asymmetry. Additional polarization observables, which carry complementary information about the mechanism, can be measured when the reaction is induced by polarized protons, as were available up to a bombarding energy of 2.9 GeV at LNS. The DISTO apparatus has thus been designed to track multiple charged products through large-acceptance detectors in a magnetic field, to provide particle identification for these products, and simultaneously to measure the incident beam polarization. The magnetic field integral used is limited by the desire to keep the detection system compact, in order to minimize the effect of pion and kaon decays in flight, and to avoid large spin precession of the incident and outgoing particles.

The same apparatus has proved valuable as well for the study of other exclusive reactions with multiple charged products, such as the meson production channels $pp \rightarrow pp\eta$, $pp\eta'$, $pp\omega$, $pp\phi$. In these cases, the mesons are tagged by detection of their charged decay products ($\pi^+\pi^-$ from η, η' and ω – in each case accompanied by an undetected π^0 – and K^+K^- from ϕ). The missing mass of the produced meson is reconstructed from momentum measurements for the two outgoing protons. The decay of the ϕ to two charged particles provides an additional measurement of invariant mass in that case.

In this paper, we give an overview of the components of the DISTO apparatus. A schematic view of the overall layout, with typical detected particle tracks, is shown in Fig. 1. The polarized proton beam from the Saturne synchrotron is incident on a liquid hydrogen target placed at the center of a large-gap dipole magnet with a cylindrically
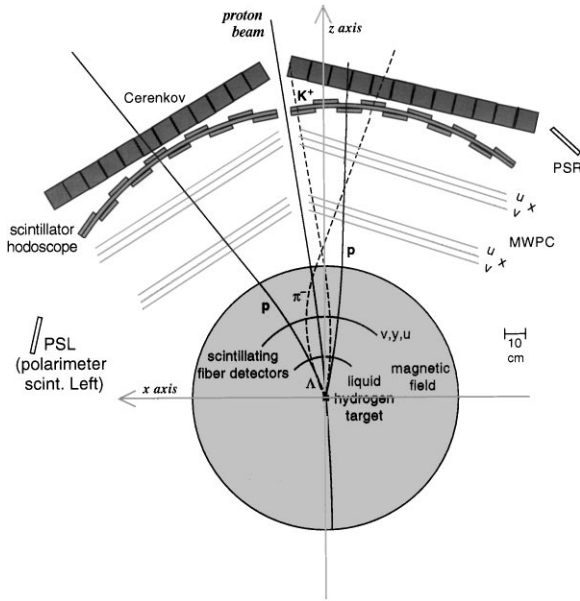
Fig. 1. Schematic layout of the DISTO experimental apparatus, viewed from above, including simulated trajectories from a pp → pK$^+$Λ event. The large shaded circle represents the effective field region. PSR and PSL are the two slabs to detect backward scattered protons in the polarimeter.

symmetric vertical field. Charged products are tracked through position-sensing chambers placed to either side of the curving beam path. Scintillating fiber arrays placed inside the magnet provide track coordinates essential for reconstructing the reaction and decay vertices (which are significantly separated for hyperon production events), as well as fast particle multiplicity information useful in defining a hardware trigger. Multi-wire proportional chambers (MWPCs) located beyond the magnet pole tips measure the exiting particle directions needed for momentum determination. A plastic scintillator hodoscope following the MWPCs also measures charged particle multiplicity for triggering purposes, and provides pulse height and timing information relevant to particle identification for each track. Further particle identification is obtained from the water Cherenkov counter hodoscope at the rear of each detector arm. All these detectors span an angular range in the laboratory frame from a few to ≈ 48°, to both sides of the beam, horizontally and ≈ ± 15.5° vertically. Extra plastic scintillating slabs are placed at large

angles on each arm, beyond the acceptance of the tracking detectors, to aid in coincidence detection of pp elastic scattering events used to monitor the beam polarization.

The properties of the beam, target and dipole magnet are summarized in Section 2, and of the individual detector components in Section 3, of this paper. The trigger electronics and data acquisition system are described in Section 4. In Section 5, we discuss general aspects of the event reconstruction and the identification of various reaction channels, and show spectra summarizing the system performance achieved under actual running conditions.

2. Beam and targets

The DISTO apparatus has been used at Saturne with polarized proton beams having kinetic energies between 1.6 and 2.85 GeV. At these energies, the beam was extracted in spills of ∼ 400 ms length every 2.0 s (at 1.6 GeV) up to every 4.3 s (at 2.85 GeV). The beam intensity has been limited to 1.0×10^8 protons/spill (far below the capacity of Saturne) by the singles rates in DISTO detectors and by the multi-particle trigger rates that could be handled with ≈ 10% dead time in the data acquisition. Beam polarizations ≳ 70% were available at all the bombarding energies used.

The beam was transported to the DISTO target through a magnetic channel tuned to ensure a minimal (2 mrad HWHM) angular divergence. The beam momentum spread at the end of the channel was ± 0.03%. The beam protons were deflected by 8.7° during passage through the DISTO dipole magnet, and by half this value by the time they reached the target.

The magnet used in the DISTO setup was originally constructed for the experiment PS170 at CERN [3]. It has a vertical pole gap of 40 cm over a radius of 50 cm. For a beam energy of 2.85 GeV, a central field strength of 1.46 T was used.

The field profile is very well characterized via mapping measurements made both at CERN [4] (with 6.0 cm step size in three orthogonal directions) and at Saturne (with 2.0 cm step size in the horizontal plane, at several vertical positions). The two sets of measurements are in excellent

agreement at overlapping points. In all, the field was mapped at seven central field strengths from 0.70 to 1.55 T, with emphasis on the upper end of this range, where saturation effects become significant. The field maps extend over the full volume relevant to the DISTO experiment. Field evaluation at all the points relevant to observed track reconstruction in the DISTO experiment was performed via smooth interpolations between the grid points of the maps and small extrapolations beyond this grid. Before the target and the detection system were installed in and around the magnet, four wire chambers were mounted along the beam path to check the validity of such calculations. Measured beam positions at various beam energies and field inductions agreed with predictions within 1 mm.

As illustrated in Fig. 2, the beam is transported up to the target in vacuum. It then travels a short distance (~ 1 cm) through air before entering a thin-walled (~ 0.07 cm), curved vacuum pipe (entrance window 10 μm of mylar) constructed from carbon fiber material. The carbon fiber pipe increases in diameter from 2.2 cm at its entrance, so as to allow detectors to be mounted within $1.5°$ of the beam over its entire length. The beam continues to travel through vacuum all the way to the beam dump, ≈ 4 m downstream of the target. The vacuum transport and the thin walls of the pipe are both intended to minimize room background rates in the detectors. The optimum beam trajectory and focusing through the system, and especially through the narrow carbon fiber pipe, is determined empirically by maximizing the ratio of pp elastic scattering events detected in the DISTO hodoscope (see Section 3.3) to the overall rate of two-particle triggers. The position and spatial width of the beam are then monitored continuously with a set of halo detectors preceding and following the target, and periodically with remotely insertable wire chamber profile monitors placed at several locations along the beam line.

Each of the halo detectors comprises four movable plastic scintillators (NE 102A) of 0.5 cm thickness and 3.0 cm² cross-sectional area, positioned to the left and right, and above and below the beam. Each scintillator and light guide are placed inside, and the corresponding photomultiplier (the ultra-
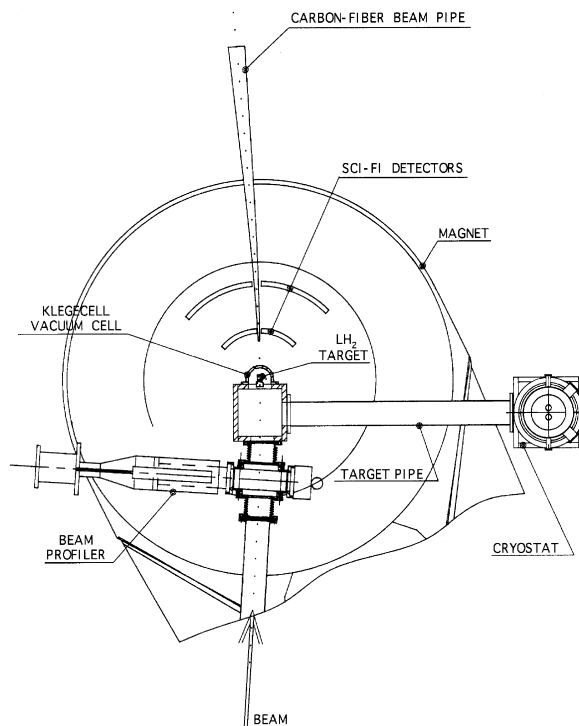

Fig. 2. Schematic layout of the liquid hydrogen target installation and of the beam path through the DISTO spectrometer magnet.

compact Hamamatsu R5600) and base outside, the vacuum, which is sealed by a rubber O-ring surrounding the base of the light guide. The photomultiplier-base assembly is furthermore contained within a metal cylinder that can be moved perpendicular to the beam axis by means of a stepping motor and a sliding vacuum seal. In addition to providing information about the beam profile, the upstream halo detector gives signals that can be used to veto reactions initiated before the beam has reached the liquid hydrogen target.

As indicated in Fig. 2, the target is located at the center of the spectrometer magnet, with its cooling and vacuum systems installed at the right side of the magnet. The whole system is mounted on rails so that it can be easily retracted to be replaced by a solid target, if needed. The liquid hydrogen volume is 2.0 cm long and 2.0 cm in diameter, contained within a cylindrical cell with a hemispherical endcap. The cell walls are made from mylar sheet of

100 μm thickness. The cell is furthermore enclosed in a vacuum chamber, whose downstream wall is a hemisphere made from Klegecell (C_2H_3Cl) of 1.0 cm thickness, located 4.3 cm from the target center. Because of the large distance between the two interaction points, events coming from beam interactions in the vacuum chamber wall can be easily distinguished, by vertex reconstruction, from events produced on the LH_2 itself. Klegecell has been chosen because of its low density, only 0.075 g/cm^3, attributable to the cellular structure of such polyvinyl chloride material.

3. Detectors

3.1. Scintillating fibers

The innermost detectors of the DISTO spectrometer are plastic scintillating fibers arranged along the surface of cylinders centered on the magnet center. The cylindrical geometry limits the range of incidence angles, and therefore of energy loss and multiple scattering, of the detected particles. The fibers are arranged in four chambers, named R0, L0 and R1, L1, surrounding the beam exit pipe at two different radii, as illustrated in Fig. 3. Each chamber comprises three planes. The central plane in each case has horizontal fibers, which measure the vertical (y) coordinate of the particle tracks, while the first and third layers measure coordinates (v and u) tilted by $\pm 45°$ with respect to y. The dimensions of each detector and
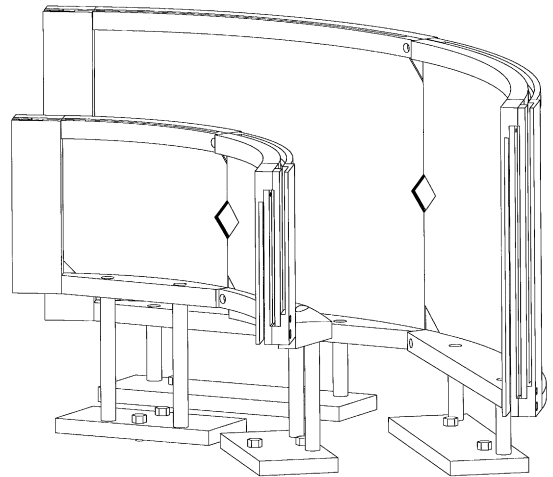

Fig. 3. Schematic drawing of the four scintillating fiber chambers and their support stands. The exit beam pipe passes through the rhomboidal holes formed where the left and right fiber chambers meet.

the number of fibers contained within each plane are specified in Table 1. In all, the chambers include nearly 3000 fibers.

The fibers, with a square cross section of 1×1 mm^2, are provided by Kuraray, type SCSF 38. Tests we made on fibers provided by various manufacturers demonstrated that fibers of square cross section give about 25% greater light output, and more uniform detection efficiency over the whole counter, than fibers of circular cross section. The chosen fiber size represents a compromise among the minimal thickness needed for a minimum-ionizing particle (MIP) to produce an acceptable

Table 1
Dimensions of the scintillating fiber detectors and numbers of fibers and position-sensitive photomultipliers used for each scintillating fiber plane

Detector	Radius (mm)	Horizontal size (mm)	Vertical size (mm)	Fibers				PSPM
				y horiz.	u $+45°$	v $-45°$	Total	Total
R0	200	157	112	112	176	176	464	6
L0	200	157	112	112	176	176	464	6
R1	400	314	224	224	368	368	960	12
L1	400	314	224	224	368	368	960	12
Total							2848	36

amount of light, the spatial resolution required of the fibers to separate Λ from Σ^0 production, and reasonable limits on the contribution to the overall momentum resolution introduced by multiple scattering in the fibers.

In order to reduce light losses and optical crosstalk between neighboring fibers, each fiber is aluminized on all surfaces except the one from which light is collected. The non-aluminized surface of each fiber is connected to a Kuraray clear light guide fiber of the same cross-sectional dimensions via a specially designed 8-pin optical connector. After the clear fibers and the scintillating fibers have been glued to the connectors, their contact surfaces are carefully polished. This procedure results in a measured light transmission coefficient of typically 80% for the optical connectors. The light guides are individually shielded, to avoid optical crosstalk, and connected via 80-pin polished optical connectors to position-sensitive photomultipliers (PSPM). We use Hamamatsu H5828 80-anode, 19-stage PSPMs, with a typical gain of 5×10^6 and moderate crosstalk among anodes. The spectral characteristics of this PSPM are well matched to the 428 nm peak emission wavelength

of the SCSF38 scintillating fibers. For diagnostic purposes, fast laser LED signals are fed to the PSPMs through 16 fibers.

The anode output signals from the PSPMs are sent to Nanometrics N-277-VG amplifier cards, and thence to a LeCroy PCOS III readout system. The discriminator thresholds are set to compromise between high detection efficiency for minimum-ionizing particles (MIPs) and low crosstalk. The crosstalk observed has both optical and electronic contributions. The chosen thresholds limited crosstalk, on average, to $\sim 5\%$ per neighboring PSPM anode, and MIP detection efficiencies to $\lesssim 70\%$. The efficiency increases with particle stopping power, as shown in Fig. 4. The efficiencies in the figure have been evaluated, for tracks detected with a minimum bias two-particle trigger and identified (see Section 5.1) as p's or π's, by eliminating one plane at a time from the track-fitting and looking for recorded hits on the eliminated plane within five fibers of the predicted track crossing.

3.2. Multi-wire proportional chambers

In order to maximize acceptance, it is desirable for the MWPCs, used to determine the particle tracks as they exit the magnetic field region, to approach the beam as closely as possible, and therefore to withstand high singles rates. Ease of construction favored the use of the planar MWPCs indicated in Fig. 1 over a cylindrical geometry similar to that of the scintillator detectors. The aluminum frames of the MWPCs maintain a minimum separation of 2.0 cm between the active area and the wall of the carbon fiber beam pipe. The set of MWPCs consists of 12 single-coordinate (v, x, or u) chambers combined into four three-coordinate blocks (henceforth referred to as "triplets"). The two smaller triplets (SV; SX; SU) are positioned at a distance of 90 cm, and the larger triplets (LV; LX; LU) at 120 cm from the center of the spectrometer magnet. The dimensions of each triplet are given in Table 2 and the wire geometry is specified in Table 3.

Each of the 12 chambers contains three layers of wire electrodes. The central layer contains anode wires of 20 μm gold-plated tungsten, held under 50 g of tension. Placed periodically within this layer
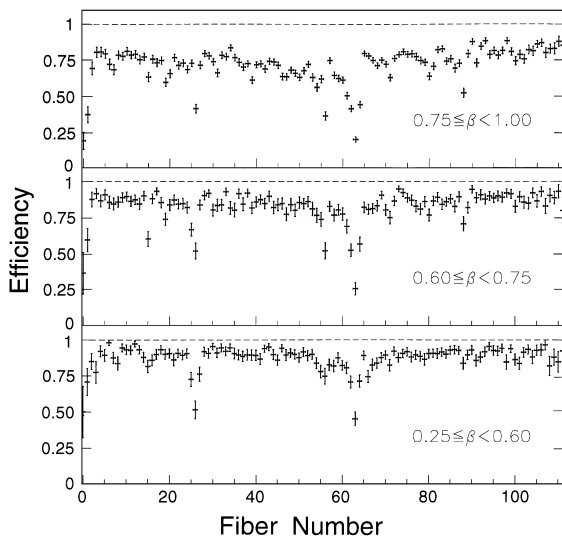

Fig. 4. Measured efficiencies vs. predicted fiber number for the y plane of the inner right scintillating fiber chamber at three different ionizing power (β) bins. The predicted elements are based on tracks fitted to information from all other detectors and planes.

Table 2
Dimensions of the MWPC's (excluding readout cards). The units are mm

Type of chamber	Max. dimensions of chambers		Fiducial region of chambers		Thickness of chambers
	Width	Height	Width	Height	
SV ; SX ; SU	979	750	869	550	25
LV ; LX ; LU	1171	1000	1061	800	25

Table 3
Wire geometry of the MWPCs. The symbols are defined in the text

Type of chamber	S_k	S_a	$W_1 - W_3$	W_2	Number of guard wires	α	Number of electronic connectors	Number of electronic channels
SX	1.5	3	6.5	3	2	90	18	288
SV	1.5	4	6.5	3	12	45	15	240
SU	1.5	4	6.5	3	12	135	15	240
LX	1.5	3	6.5	3	2	90	22	352
LV	1.5	4	6.5	3	23	45	19	304
LU	1.5	4	6.5	3	23	135	19	304

are guard wires of 100 μm copper–beryllium held under 100 g of tension. The same wire is used for the two surrounding cathode planes. Each chamber is isolated from the others and from the environment by aluminized mylar entrance and exit windows, with 50 μm mylar and 10 μm aluminum thickness. The detailed wire geometry, including the number of anode wires, for each chamber type is summarized in Table 3.2, in which the symbols are defined as follows: $S_{k(a)}$ represents the pitch of the cathode (anode) wires (in mm); $W_1 - W_3$ is the distance (mm) between the cathode wires and the mylar windows, while W_2 is that between the anode and cathode wire planes; α is the orientation angle of the signal wires with respect to horizontal. Due to the length of the wires, up to three nylon strings, 0.3 mm in diameter, have been used within each chamber to provide mechanical support for the cathode and signal wires.

The chambers are operated with an argon–isobutane gas mixture. The operating high voltage is decreased by 500 V during the spill-off period. Their performance is stable, with typical efficiencies $\gtrsim 95\%$ per plane, when 1.0×10^8 protons per beam

burst are incident on the 2-cm thick LH_2 target. Under these conditions an estimated instantaneous rate $\gtrsim 1.0 \times 10^5$ particles/cm^2 s is reached near the beam. Although bad beam bursts occasionally led to excessive currents that tripped off several chambers, they generally recovered very quickly. The chamber information is read out with the same LeCroy PCOS III system used for the scintillating fibers. Nanometrics N-277-C preamplifier/discriminator cards with a modified, increased input impedance are used on the chambers to feed the PCOS electronics.

3.3. Scintillator hodoscope

The DISTO hodoscope is made from 32 slabs of plastic scintillator (1.9 cm thick) comprising 10 straight vertical "x" elements (12.2×80.4 cm^2) and six curved horizontal "y" elements (13.2 cm × 117.4 cm arc length) per arm. The two arms are arranged symmetrically to the left and right of the carbon fiber beam pipe, with the active area of each extending to $\pm 1.5°$ of the central axis of the pipe. The y-elements follow the surface of a cylinder at

a radial distance of 143 cm from the magnet center. The x-elements are mounted alternately 2.5 cm in front of and 2.5 cm behind the y-elements. The overlap of the "x" and "y" slabs defines pixels of 13.2×12.2 cm^2.

The scintillator hodoscope serves several purposes: it provides the main charged particle multiplicity measurement for use in the hardware trigger and determines the trigger start time; its pulse height and relative arrival time information for different tracks allow partial particle identification (supplemented by the Cherenkov detectors, see Section 5.1); the matching of arrival times for hits in x and y elements permits confirmation of the coupling of hits on different planes of the tracking detectors; and the correlations between the pixels fired by charged particles on the left and right arms allow simple programmable logic triggers to select data samples enriched in specific two-body reaction events. An example of the latter type of correlation is shown in Fig. 5 by data collected at 1.6 GeV bombarding energy with a general two-body trigger. A crude coplanarity condition was imposed in the logic for this trigger, by requiring that a particle falling in the upper-half of the hodoscope on one arm be in coincidence with a particle in the lower-half on the other arm. This trigger requirement is responsible for the "checkerboard" pattern observed in the histogram in Fig. 5. The numbering of pixel indices was chosen to yield a simple and prominent diagonal locus reflecting the angular correlation of pp elastic scattering events. During normal operation of the experiment, such correlations are used to define a selective elastic scattering trigger for a fraction of the beam bursts, to provide online monitoring of the beam polarization (see Sections 4.1 and 5.2).

Pulse height and timing information from the hodoscope are digitized in LeCroy FERA ADCs and time-to-amplitude converters. Electronics costs were minimized by mounting photomultiplier tubes on only one end of each hodoscope element, and by using leading edge (instead of constant fraction) timing discrimination. This approach necessitates software corrections to the readout times and amplitudes from the correlations among signal arrival time, pulse height and distance of the impact position from the phototube. In situ calibrations of these correlations are aided by the hodoscope geometry, which provides a narrow (0.5 cm width) overlap region between each pair of adjacent x-elements, whose phototubes are mounted alternately at the top and bottom ends. For tracks crossing these overlap regions, the time difference between signals in the two fired x-element phototubes can be correlated with the y impact coordinate deduced via ray-tracing from the tracking detectors. Moreover the pixel structure of the hodoscope allows one to establish the time correlations between the x and y struck elements. Then the relative timing offsets of different phototubes and the time–position correlations can be obtained. Corrections to the leading edge timing were established in test runs where both leading edge and constant fraction discrimination were used for a subset of the hodoscope elements. After software corrections, the arrival time difference between two particles at the hodoscope can be measured with a typical resolution σ of 800 ps.

As indicated in Fig. 1, an eleventh vertical scintillator slab has been added to each hodoscope arm, beyond the horizontal acceptance of the tracking detectors. These slabs are used only in the definition of polarimeter triggers (see Section 4.1), where
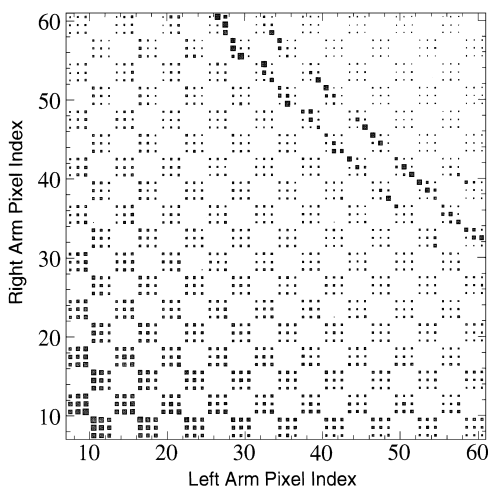

Fig. 5. The raw distribution of left vs. right hodoscope pixels fired in coincidence by events at 1.6 GeV passing a generalized two-body trigger described in the text. Elastic scattering events are clearly visible as the enhanced diagonal locus near the upper-right corner.

they detect large-angle recoil protons from pp elastic scattering in coincidence with forward protons that fall well within the normal acceptance on the other arm. The left–right asymmetric placement of the extra slabs on the two detector arms allows, after software conditions, for nearly symmetric acceptance of the desired events, in light of the significant bending of the large-angle protons in the spectrometer magnet. These extra plastic scintillators are rectangular (18 cm × 92 cm) in cross section and of 1.0 cm thickness. They each have photomultipliers mounted on both the bottom and top ends, in order to provide a time difference useful in constraining the coplanarity of the selected events (see Section 5.2). Their pulse heights and times are also digitized in FERA ADCs.

3.4. Cherenkov detectors

The final detector wall on each arm consists of 12 adjacent water Cherenkov counters, similar to the ones described in [5]. Each is built of a rectangular aluminum container of external dimensions 90 cm × 10 cm × 10 cm, with 2 mm wall thickness, filled with de-ionized water, to which is added a small amount of wavelength shifter (8 mg/l polyphenyl 1 from Lambda Physik GmbH). The walls are covered with white millipore paper to reflect the Cherenkov light, which is detected by two 7.6 cm diameter photomultipliers. The photomultipliers and bases are mounted at both ends of the detector module, separated from the water by lucite windows. Digitization of the 48 analog and 48 time signals is performed in FERA electronics.

The measured efficiency of the water Cherenkov detectors as a function of particle velocity is shown in Fig. 6 for tracks reconstructed from the DISTO detectors. The velocity β was estimated for each track by identification of the particle with the dE/dx information from the hodoscope and the momentum determined from the tracking. The Cherenkov threshold ($\beta_{thr} = 1/n_{H_2O} = 0.75$) is smeared out in the figure due to the momentum resolution. The number of photoelectrons detected for a particle with $\beta \approx 1$ can be determined from a Poisson fit to the light output distribution for fast pions. The measured mean number of photoelectrons per detector module is greater than 60.
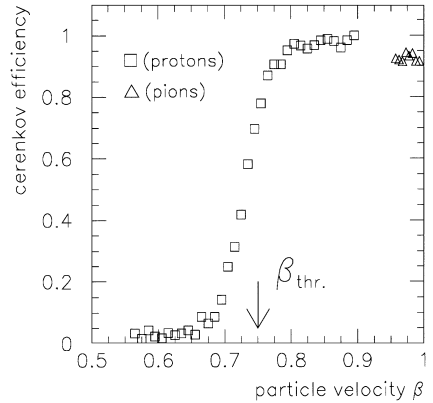

Fig. 6. Efficiency of the Cherenkov detector as a function of the particle velocity β for protons and π^+. The slightly lower π^+ efficiency is due to contamination of the selected sample by slower protons. The Cherenkov threshold is shown, too.

4. Trigger electronics and data acquisition

4.1. Trigger logic

A number of different hardware triggers can be easily programmed for the DISTO detectors. Furthermore, different logic requirements can be downloaded to the trigger modules for different beam bursts during a single run. All triggers used were based on fast signals from the scintillating fiber and the plastic hodoscope detectors only. In normal data-taking mode, the trigger was changed periodically between a multi-particle reaction selector used for the majority of beam spills and a polarimeter trigger used for the remainder. Both of these are described below. We will not describe in detail a number of auxiliary triggers that were used for diagnostic purposes.

The multi-particle trigger is designed to allow acquisition of all reactions with four charged prongs within the detector acceptance. In order to limit readout dead time to $\approx 10\%$, the hardware trigger rate must not exceed 3000 events/spill (corresponding to an instantaneous rate of 7.5 kHz). These goals are accomplished for a luminosity of 1.0×10^{31} cm^{-2} per spill by requirements on the scintillating fiber and hodoscope hit multiplicities. In particular, at least seven hodoscope elements must be fired, in a pattern that allows for two tracks to cross the same x or the same y element. We

accommodate the inefficiencies in the scintillating fibers by demanding only 3 or more hits at the outer chambers, while the inner chambers must register at least 2 hits, permitting events where, for example, a Λ decays beyond 20 cm from the target. The primary multiplicity requirements for the scintillating fibers are imposed only on the combined (left + right) y-planes. We place an additional minimal condition on the u and v planes, demanding at least one hit on the left and right arms combined, for both the inner and outer chambers. The trigger is then the coincidence among all these requirements. The rather stringent hodoscope logic minimizes the number of spurious triggers caused by crosstalk in the scintillating fibers, although it does still pass a small fraction of three-particle events, by virtue of the narrow overlap region between adjacent x-elements.

The scheme of the trigger logic is shown in Fig. 7. The front-end signals given by each detector are shown in the left part of the figure. Different processing techniques are applied to the raw signals given by the triggering detectors in order to match the information with the trigger hardware setup. The hodoscope analog signals (R4 and L4) are directly sent to the counting room where they are processed by commercial programmable CAMAC discriminator and delay modules.

The information from the fibers is processed near the detectors before being sent to the counting room. The processing is different for the y and for the u and v planes. The y planes feed specially designed "Current Adder" NIM modules, described in detail in Ref. [6], that generate a shaped 2 mA signal (i.e. 100 mV on 50 Ω resistor) per hit fiber. These modules, together with commercial linear fan-in/fan-out, generate a current signal proportional to the input multiplicity. The current signal given by the y plane of each fiber chamber feeds a home-made "dual threshold discriminator" (DTD) CAMAC module, described in Ref. [7]. The module has four independent outputs, each of which gives a "true" logic signal when the input falls within a corresponding voltage window defined by two software programmable thresholds. Since the low and high thresholds are independently programmable, any y-plane multiplicity configuration can be selected.
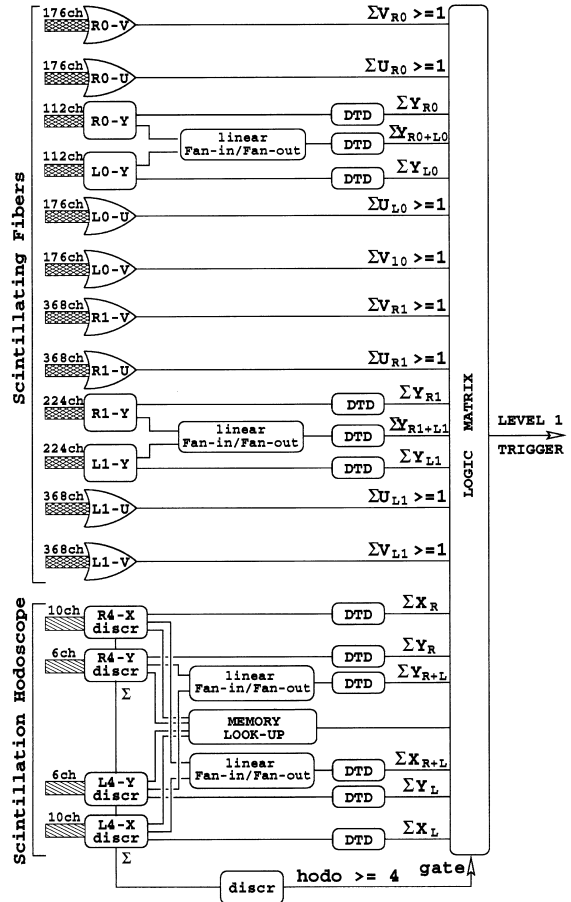

Fig. 7. Logic layout of the DISTO trigger.

In contrast, the signals from the u and v fiber planes are simply OR-ed using the internal wired-or facility of PCOS latches. The overall logical OR from each u and v plane is then sent to the counting room, where the trigger can then demand only that at least one hit be registered on the corresponding fiber plane.

The DTDs and a special version of Current-Adder modules (without the internal shaper) are also used to get multiplicity information from different planes of the scintillation hodoscope. The logic signals from the fibers and the hodoscope feed three commercial Logic Matrix Units, each of which permits programming of up to eight different logical combinations (AND, OR, AND/OR mixed logic) of its 16 input signals.

An additional circuit, not shown in Fig. 7, was used to synchronize the data acquisition with the time structure of the Saturne beam: spills of 0.4 s duration arriving every 4.3 s at the maximum energy of 2.85 GeV.

The final critical part of the trigger electronics are two commercial Programmable Lookup Units, which process logic signals from selected hodoscope x and y elements. These units facilitate the selection of events satisfying detailed correlation patterns between hodoscope elements on the left and right arms. They are used for the polarimeter trigger to pick out events consistent with pp elastic scattering into four specific angle regions, which provide left–right symmetric coincidence coverage of two c.m. angle bins. By imposing this correlation in the hardware, we have scaler signals character-

ized by a sizable analyzing power available to monitor the beam polarization for *every* beam spill, while the polarimeter trigger is used for full event recording typically in only 10–20% of the spills.

A user-friendly software package [6] to download multiplicity thresholds and logic programming enhances the flexibility of the trigger hardware, and allows the trigger configuration to be changed from one beam spill to the next.

4.2. Data acquisition system

The DISTO data acquisition system (DAQ) has been described in detail in Ref. [7]. Its overall architecture is illustrated schematically in Fig. 8. The system is based on a VME 68030 CPU running the OS/9 operating system, housed in a single VME
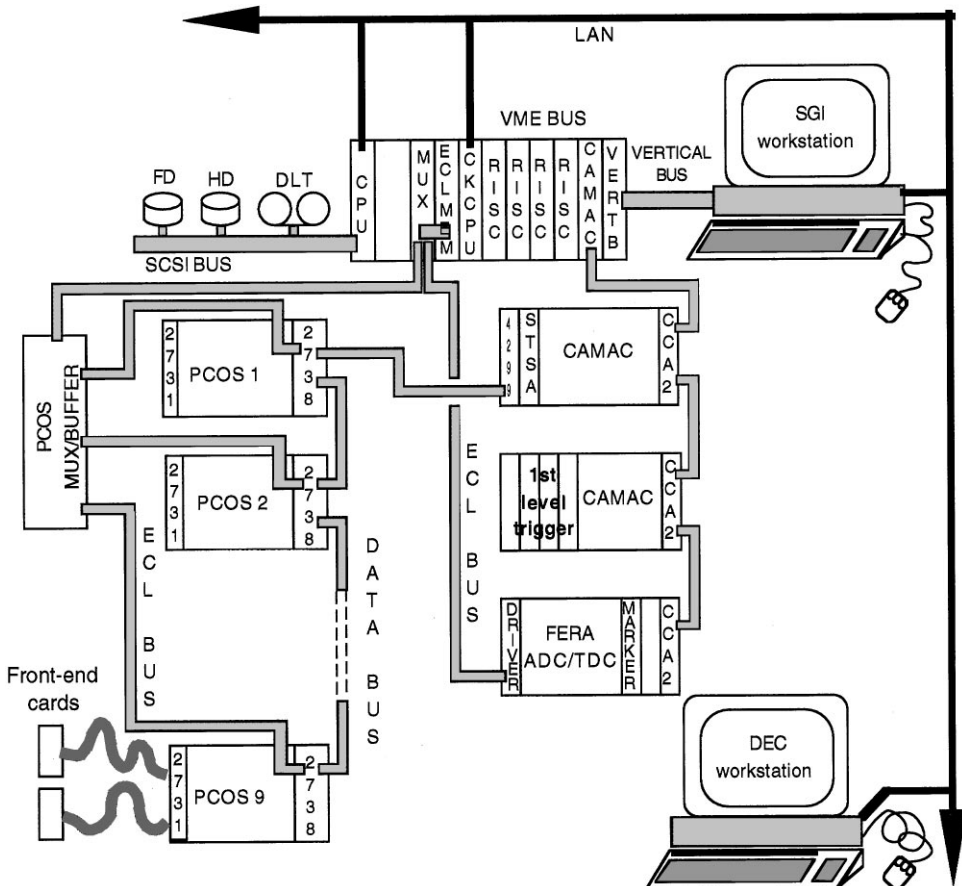

Fig. 8. Components of the DISTO data acquisition system.

crate together with a CAMAC interface, a triple-port ECL memory buffer with 3×1 MB storage, and four RISC R3000 CPUs. An additional VMEbus CPU operates as an event server, transmitting data to workstations.

The ECL outputs from different crates, containing digitized hit addresses from all the PCOS latches within each crate, are recorded *in parallel* in a specially designed FIFO/multiplexer module, which then writes them sequentially to a single ECL output port, for transmission to the VME memory buffer. This readout scheme avoids timing problems we experienced when the outputs of more than five PCOS crates were connected together in a single daisy chain. Digitized pulse height and timing information from the ten FERA (LeCroy model 4300B) ADCs is read out through a LeCroy model 4301 FERA Driver module. ADC channels with zero or overflowed outputs are suppressed in the readout.

A typical event acquired with the multi-particle trigger described above contains about 250 bytes of information from the PCOS III (for fiber and wire chambers) and FERA (for scintillator hodoscope and Cherenkov counters) readout electronics.

The DAQ system was designed to take advantage of the beam time structure at Saturne to read out the data at maximum speed. During each beam spill, data from the PCOS and FERA readout electronics is transmitted directly, via an ECL bus, to the memory buffer under the control of a hard-wired 10 MHz sequencer. The data acquisition CPU is used only at the end of the spill to transfer the accumulated contents of this buffer and of various scalers to a free RISC CPU, which can be used to implement a second-level trigger. Data is recorded on a digital linear tape (DLT) drive which is connected to the SCSI port of the data acquisition CPU.

Two UNIX workstations are connected to the VME CPUs through a fast parallel bus and the Local Area Network. The VME CPUs and the workstations share the same disks using NFS protocol. The workstations allow on-line monitoring of a sample of the recorded events, as well as user control of the acquisition process and of trigger and readout electronics setup. The on-line programs are written in FORTRAN and C code, and the monitoring is based on the PAW system [8] developed at CERN.

Under normal operation, the VME memory buffer has the capacity to store up to 11 000 multi-particle trigger events per beam spill. In practice, the data acquisition rate was limited to roughly one-quarter of this capacity by dead time incurred in the FERA readout. Since the hardware trigger rate is limited by this front-end dead time to a value that does not stress the DLT cassette recording of the data, it has proved unnecessary to impose a more restrictive second-level trigger in the RISC processors.

5. System performance

The performance of the DISTO detectors can be illustrated by spectra of particle momenta, reaction angles, invariant and missing masses, etc., reconstructed from the events recorded with both two-body and multi-particle triggers.

Two codes have been developed independently for event reconstruction: one (hereafter referred to as the HYP code) was optimized to study reactions with hyperon production, where particles can stem from two or more vertices, and information from the scintillating fibers is critical in locating the vertices; the second (the MES code) was optimized for the reconstruction of reactions where all the detected particles originate from a common vertex, which can be reconstructed from MWPC hits even in the absence of scintillating fiber information.

The two codes produce consistent results in the analysis of data taken with two-body triggers, and of data for the meson production channels $pp \rightarrow pp\omega, pp\phi$. In addition, both codes have been checked by applying them to simulated data generated with the same event structure as the real detector readout. The simulations were performed within the GEANT framework [9], utilizing both the standard phase space generator and alternative generators based on published reaction data or theoretical models. The intersection hits of the generated tracks with the DISTO detectors were digitized incorporating realistic resolution functions and, in the case of the scintillating fibers,

crosstalk and noise patterns extracted from the actual data obtained with beam. Such simulations permit realistic assessment of acceptances and reconstruction efficiencies for the various reaction channels of interest.

5.1. The retracking programs

In this section, we present spectra reconstructed utilizing both the HYP and MES retracking programs. Both codes provide

- pattern recognition, that is association of the recorded hits to the proper track;
- determination of the momenta of each particle;
- particle identification;
- reconstruction of the vertices from which the tracks originate;
- full kinematic reconstruction of the reaction under study.

Pattern recognition was complicated by crosstalk, noise, and inefficiencies in the scintillating fiber detectors. It was therefore based in both codes, as a first approach, on the hits provided by hodoscope pixels and wire chambers. These detectors were in a region where the magnetic field is so low that linear interpolations are justified as a starting approximation.

5.1.1. The HYP code

In this code, one first concentrates on hits recorded in the MWPCs and the scintillator hodoscope. These hits are sorted into linear track segments, of which we demand consistent information from the u, v and x planes of the MWPCs (for those tracks where all three are available) and consistent x- and y-element times from the hodoscope (when other tracks do not appear to share one of these elements). The sign of a particle's charge can already be determined clearly from these track segments, since positive and negative tracks fall along quite distinct loci in the correlation of x-coordinates at the inner and outer MWPCs.

One next approximately extrapolates the track segments reconstructed outside the magnet inward toward the center of the target. Only those recorded fiber hits that fall sufficiently close to the ones predicted from these track extrapolations are

used to constrain the first-pass track fitting. The detailed field map of the spectrometer magnet is taken into account in fitting appropriate curved trajectories to the extracted hit coordinates, using an algorithm based on the CERN library routine MOMENTM [10]. This algorithm does not yet have allowance for particle energy loss or multiple scattering along its path. The fitted tracks resulting from the first pass are then used to locate additional relevant fiber hits that may have been missed earlier due to the crudeness of the original track extrapolations. Any two fitted trajectories are then extrapolated inward through the field from their first recorded hits, to find the location of their minimum three-dimensional separation. An indication of the vertex resolution obtained in this way is shown in Fig. 9, by the distribution of events collected with a general two-body trigger with respect to the z-coordinate of the reconstructed vertex. (The z-axis is chosen parallel to the incident proton's path before it enters the spectrometer magnet.) The two clearly separated peaks seen in this spectrum correspond to the 2-cm-thick LH_2 target and to the 1-cm-thick Klegecell exit window from the target's vacuum chamber (see Section 2). The peaks seen are consistent with the known
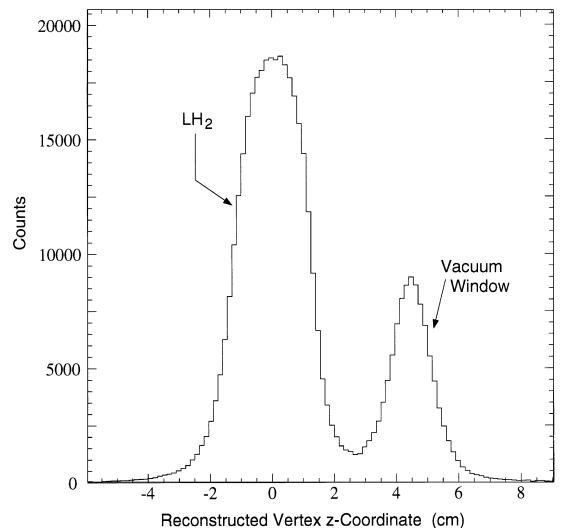

Fig. 9. Longitudinal distribution of reaction vertices reconstructed from retracking of events obtained with a generalized two-body trigger. Peaks corresponding to the LH_2 target and to the Klegecell vacuum window are prominent.

thicknesses when convoluted with a vertex z (rms) resolution of several mm.

Elastic scattering events can be picked out clearly from the general background arising from detection of two charged particles by means of the angular correlation of the reconstructed tracks, as seen in Fig. 10. The polar and azimuthal angles plotted in these spectra are evaluated at the reaction vertex, and the elastic loci are prominent. The resolution is particularly good for the coplanarity ($\sigma \approx 0.7°$ in the difference of the two azimuthal angles vs. $1.5°$ in the opening angle), since the vertical projection of each track is only weakly correlated with momentum uncertainties. Conditions on the opening angle and coplanarity produce a sample of elastic scattering events with little background, for which one can then compare the reconstructed momenta for each event to those expected kinematically for the reconstructed scattering angles. The resulting spectra of the relative momentum error are shown for the left and right arms separately in Fig. 11. The $\delta p/p$ resolution obtained in Fig. 11 has contributions from the resolution of the polar scattering angle measurements and from the beam energy spread, as well as from the momentum resolution. Utilizing estimates of the first two contributions, we infer an overall relative momentum resolution $\sigma \approx 5\%$ for particle momenta between 1.5 and 2.5 GeV/c.

For data stored with the multiparticle trigger, the detailed matching criteria used to assign fiber hits to tracks, and the handling of ambiguities, have been tuned to optimize the reconstruction efficiency for hyperon production ($pp \rightarrow pK^+Y$) events, where analysis of the displaced reaction and decay vertices demands efficient winnowing of fiber information. In this section, we show typical spectra obtained from events where the above algorithm succeeds in reconstructing four charged
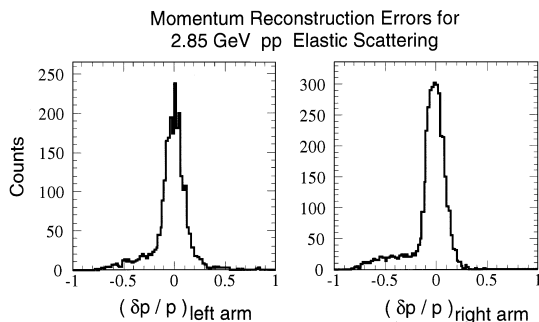

Fig. 11. Distribution of events passing 2.85 GeV elastic scattering conditions on opening angle and coplanarity, with respect to the fractional deviation of the reconstructed momentum from the kinematically predicted momentum on each detector arm. The kinematic prediction is based on the reconstructed scattering angle for the track on that arm.

tracks – each with information from at least one fiber chamber – that appear to diverge from two displaced vertices.

Particle identification can be deduced from the correlation of Cherenkov and/or hodoscope pulse height with the reconstructed particle momentum. The correlations observed for tracks of positive curvature are shown in Fig. 12. The fitted tracks have been used to remove uninteresting pulse height variations associated with different path lengths through the counters and with different light attenuation from the impact position to the phototubes. Furthermore, pileup effects have been removed from Fig. 12 by eliminating the contributions from detector elements crossed by two or more fitted tracks. Intense and reasonably separated π^+ and proton groups are seen in the raw data for both Cherenkov and hodoscope counters. The K^+ band falls in the middle, and is revealed clearly only by the addition of conditions on other observables, e.g., by requiring that the event contain proton and π^- tracks characterized by an

Fig. 10. Angular correlations of events acquired with the general two-body trigger at 2.85 GeV. In the polar angle correlation in the left-hand frame, the elastic scattering locus stands out very clearly above background. The solid curve represents kinematics for 2.85 GeV elastic scattering. Elastic events are also clearly identifiable by the coplanarity peak at 180° in the right-hand spectrum.

Fig. 12. Correlations observed between the momentum reconstructed from fits to positive-curvature tracks emerging from the reaction vertex and the corresponding pulse height recorded in the Cherenkov or hodoscope counters. Data from all counters are included in these histograms. The raw spectra in the upper frames are dominated by distinct proton and π^+ groups. A K^+ group of comparable intensity to the others can be seen in the lower frames, after requiring that the tracks from the other vertex give an invariant mass consistent with Λ decay.
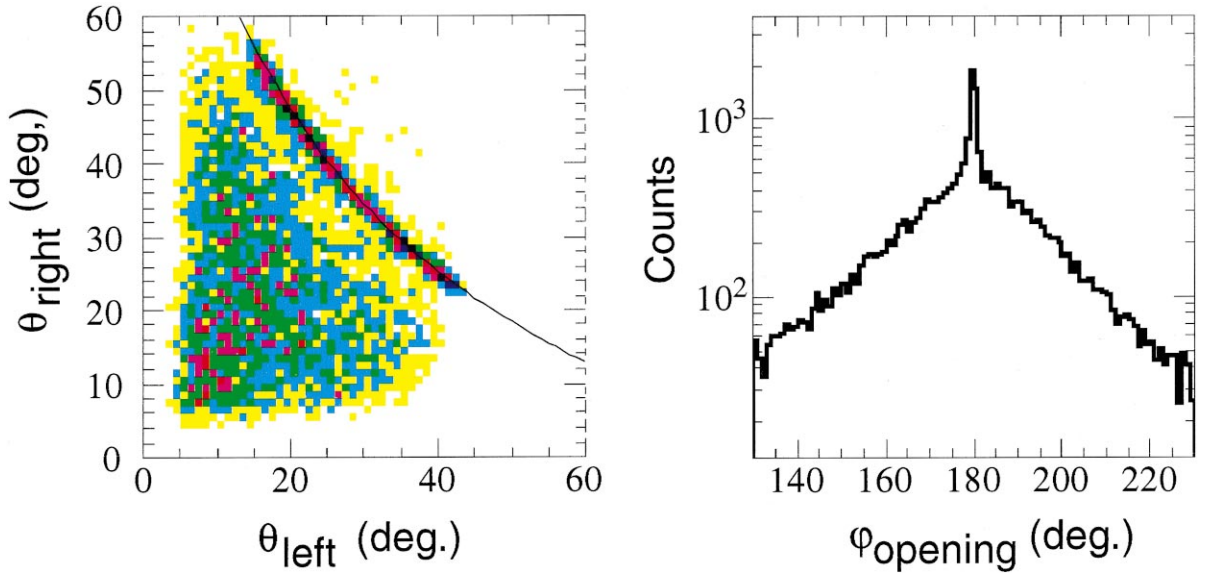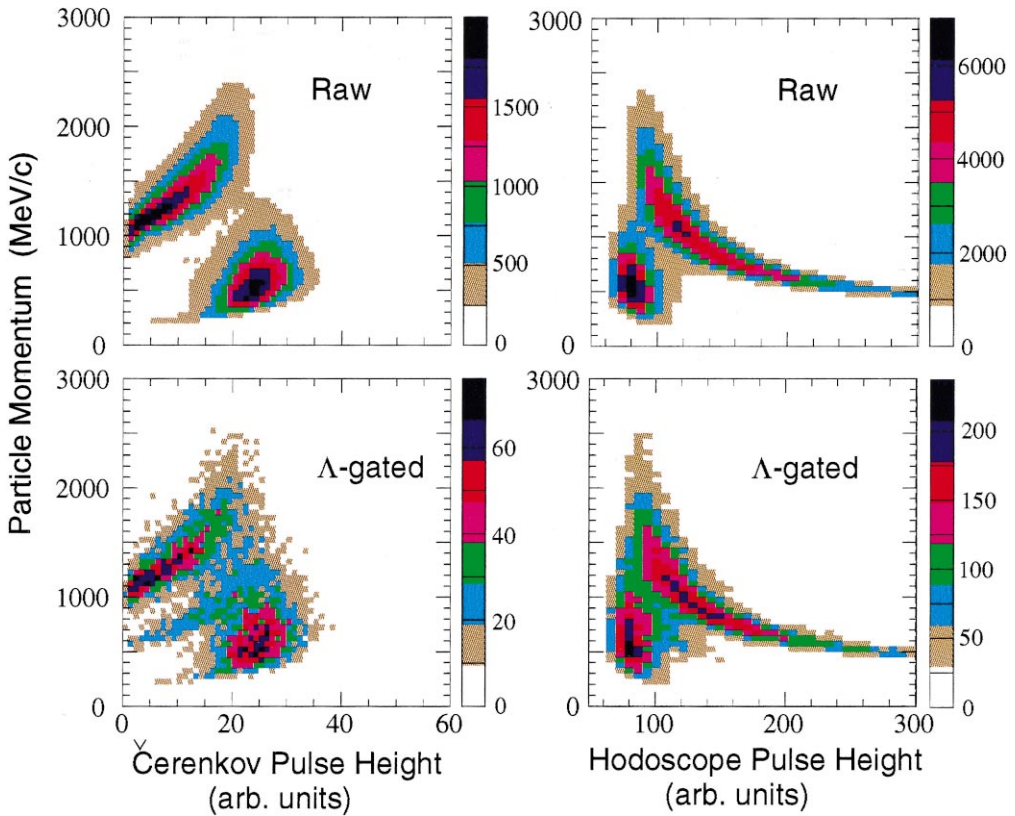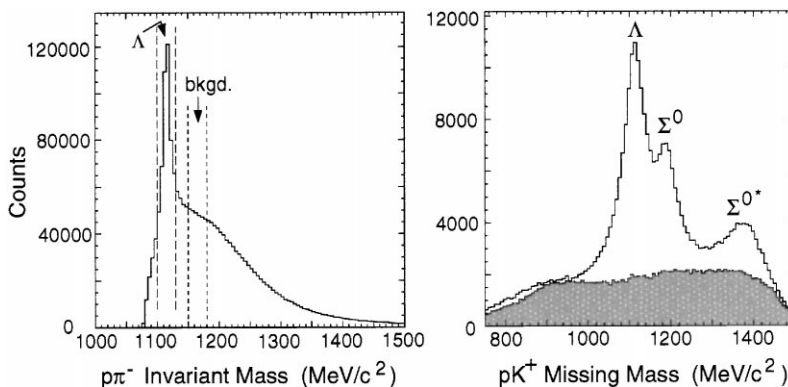
Fig. 10.

Fig. 12.

Fig. 13. Spectra of invariant and missing mass reconstructed, respectively, from the decay daughters and from the reaction products for multi-particle events that pass loose conditions designed to emphasize hyperon production. The missing mass spectra include events which fall within the Λ invariant mass gate shown, or (shaded portion) within the background gate of equal width.

invariant mass consistent with the mass of the Λ. While the π, K and p groups are not fully resolved in Fig. 12, unambiguous particle assignments can be made in the vast majority of events by utilizing pulse height information from both Cherenkov and hodoscope detectors, hodoscope time differences among tracks, and kinematic constraints.

The resolutions obtained in invariant and missing mass reconstructions are illustrated by the spectra for pKY candidate events in Fig. 13. At the vertex reconstructed from p and π^- tracks, we see the Λ invariant mass peak clearly, with a resolution $\sigma \simeq 5\,\text{MeV}/c^2$. The background in this spectrum arises predominantly from abundant multiple pion $(\pi^+\pi^-, \pi^+\pi^-\pi^0)$ production processes, in which a π^+ has been misidentified as a K^+. The background could be strongly suppressed, at the expense of removing a small fraction of the Λ production events, by placing additional gates on the overall (4-track) missing mass and on the minimum separation of the decay from the reaction vertex.

Also shown in Fig. 13 is the spectrum of missing mass reconstructed from p and K^+ tracks, for events falling within either the Λ or the background gates indicated in the invariant mass spectrum. When the background is subtracted, the resulting missing mass spectrum shows very clear peaks corresponding to the direct production of $\Lambda(1116)$, $\Sigma^0(1192)$ and $\Sigma^{0*}(1385)$. At the present stage of

the analysis, the former two peaks have an instrumental resolution (averaged over all phase space) of $\sigma \simeq 25 - 30\,\text{MeV}/c^2$, so that they are barely resolved from each other. Resolution improvements under way include a simultaneous refitting of all tracks for pKY candidate events, incorporating kinematic constraints on the event and some allowance for particle multiple scattering in the scintillating fibers. Events between the Σ and Σ^* peaks are presumably due to continuum $pp \to pK^+\Lambda\pi^0$ reactions.

Finally, Fig. 14 shows simulation and measurement results relevant to the acceptance of the DISTO apparatus for hyperon production events. The first frame shows the Dalitz plot expected for $pp \to pK^+\Lambda$ reactions, from a simulation based on the assumption of a uniform phase space population in the reaction mechanism. The simulation includes the same trigger logic as the experiment, together with models of the resolution, inefficiencies and crosstalk of the detectors. Only those simulated events successfully reconstructed by the analysis code have been included in the plot. The acceptance of the DISTO setup leads to the sparse population of the upper-half of the Dalitz ellipse seen in the figure.

The second frame of Fig. 14 compares measured and simulated Λ decay distributions relevant to the determination of the Λ's polarization component along a quantization axis normal to the production plane of the Λ (i.e., along $\hat{n} \| \mathbf{k}_{\text{beam}} \times \mathbf{k}_\Lambda$). The relevant
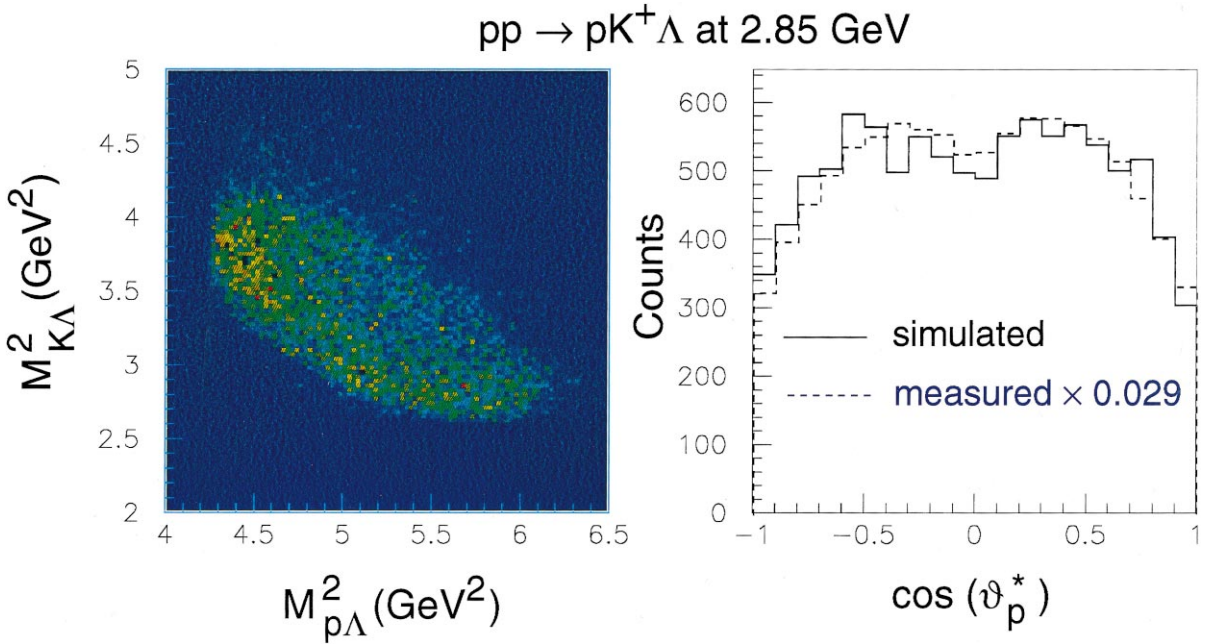
Fig. 14. Distributions indicating the phase space acceptance of the DISTO spectrometer for exclusive pp → pK$^+$Λ events at 2.85 GeV bombarding energy. On the left is the Dalitz plot for events simulated assuming uniform phase space density, when those events are successfully reconstructed. The events falling beyond the kinematically allowed ellipse result from misidentifications in the event reconstruction. The right-hand frame shows simulated and measured distributions with respect to the daughter proton emission angle within the Λ rest frame. The simulations assumed unpolarized Λ production. The measured spectrum includes signal as well as background events within the Λ invariant mass gate shown in Fig. 13, and is summed over both beam spin directions and Λ detection to both the left and right of the beam direction. It has been scaled by a factor 0.029 to permit direct comparison with the simulation.

variable is the cosine of the daughter proton's emission angle with respect to this quantization axis, deduced in the Λ rest frame. A Λ polarization would be manifested by a fore–aft asymmetry in this distribution. The simulations are based on un-polarized Λ's, and they show a symmetric, though not quite isotropic, coverage of the decay phase space. The dips seen when |cos θ*| is near unity occur because the daughter π$^-$ are then no longer fully contained within the vertical acceptance of the detectors. The small dip near cos θ* = 0 arises be-cause in this region the daughter proton and pion often cross the same hodoscope y-element, reduc-ing the trigger efficiency. The measured cos θ* dis-tribution agrees well with the simulations.

5.1.2. The MES code

A second tracking algorithm has been optimized for the reconstruction of reactions where all par-ticles originate from a common vertex. This is the case for the vector meson production channels of interest. This particular algorithm introduces a constraint by assuming the tracks to originate at a common vertex in the target region, allowing less stringent demands to be placed on the information from the scintillating fiber chambers. Indeed, it is even possible to reconstruct appropriate events fully without utilizing any fiber hits. As a first step, a search for correlated hit points is performed, requiring at least two coordinates per MWPC trip-let, as well as a hodoscope pixel. In a subsequent step, the tracks are refit to share a common vertex. For the fits, the routine MOMENTM [10] is re-placed by a fast multi-dimensional table lookup and interpolation algorithm.

As an example of an analysis using this algo-rithm, Fig. 15 shows the invariant mass distribu-tion of reconstructed pp → ppK$^+$K$^-$ events at
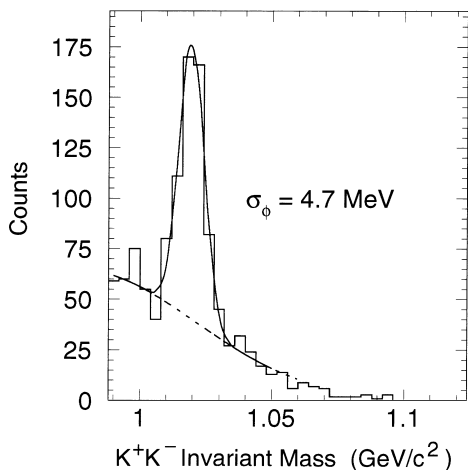
Fig. 15. Invariant mass distribution of K$^+$ K$^-$ pairs detected at 2.85 GeV bombarding energy, after imposition of tight conditions selecting four-particle ppK$^+$K$^-$ final states. The ϕ signal is clearly visible, superimposed on a background of non-resonant K$^+$ K$^-$ (and some leakthrough $\pi^+\pi^-$) pairs. The spectrum has not been corrected for the variation of acceptance and efficiency with invariant mass. The indicated width of the Gaussian fitted to the ϕ peak includes contributions from detector resolution and from the intrinsic width of the ϕ.

2.85 GeV. A clear peak signaling ϕ production is observed. Tight K$^\pm$ particle identification gates imposed on the correlation between particle momentum and Cherenkov counter pulse height were crucial to reveal this weak reaction: they served to suppress $\pi^+\pi^-$ background by nearly three orders of magnitude. A parallel analysis of ϕ production with the HYP code yields a quite different reconstruction efficiency, due to the extra requirements on scintillating fiber hits and the additional use of hodoscope pulse heights for identification of low-momentum kaons. However, when the reconstruction efficiencies of the two codes are evaluated by applying them to simulated ϕ production events, the two analyses give consistent ϕ yields within their respective systematic uncertainties.

5.2. Polarimeter trigger results

In order to monitor the beam polarization continuously throughout DISTO measurements, we have used pp elastic scattering, for which analyzing power measurements have been previously made in the vicinity of 2–3 GeV with both polarized beams

and polarized targets [11,12]. Clean event identification requires coincident detection of both protons, while minimization of instrumental asymmetries in the polarization determination favors a setup that has at least approximate left–right symmetry. However, as seen from Fig. 10, the normal DISTO detector acceptance provides, at 2.85 GeV, only a limited angle range ($23° \leq \theta_{lab} \leq 43°$) over which the scattered protons can be detected on *either* arm. This leaves only a single c.m. angle range, centered about $\theta_{c.m.} \approx 71°$ or four-momentum transfer $-t \approx 1.8$ (GeV/c)^2, where A_y is sizable (≈ 0.18) and we have left-right symmetric coverage; the forward proton is then detected in the laboratory range 22.5–25.5° on the left or right, and the coincident backward proton at 40–44° on the other arm. Unfortunately, the elastic scattering cross section is rather small at such large momentum transfer.

For this reason, we have supplemented the normal DISTO detectors with the extra large-angle scintillators described in Section 3.3. These detect the recoiling protons on the left or right side that are in coincidence with forward protons detected on the other arm at $13.0° \leq \theta_{lab} \leq 15.5°$, centered about $\theta_{c.m.} \approx 44°$ and $-t \approx 0.75$ (GeV/c)^2. Here A_y is nearly as large as in the $\theta_{c.m.} \approx 71°$ bin, but the lab-frame differential cross section is about a factor of 20 larger [11,12].

The recoil protons that end up in the extra scintillating slabs fall beyond the acceptance of the tracking detectors. We therefore have momentum information and high-resolution angle measurements available only for the forward proton, to use in software conditions selecting elastic scattering events. In addition, however, a crude coplanarity condition can be imposed, by virtue of the vertical position information provided by the time difference between signals in the top and bottom phototubes on the large-angle scintillators. The strong two-body correlation between this position and the azimuthal angle deduced from tracking of the forward proton is shown in Fig. 16. In practice, we find that a software gate on this correlation, in combination with one on the forward proton's momentum vs. polar angle, is sufficient to discriminate against the non-elastic background in this angle region.
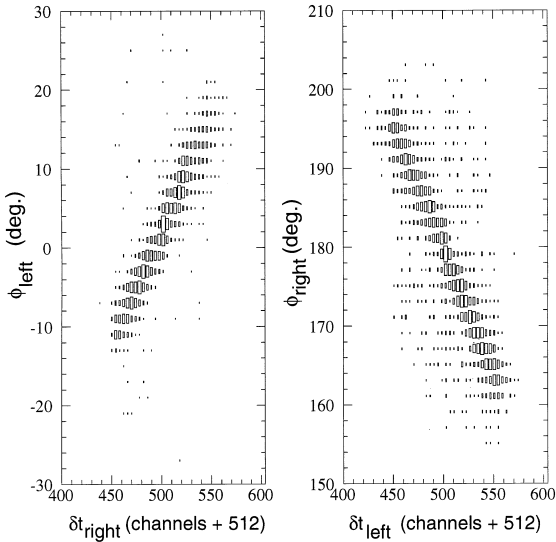
Fig. 16. Coplanarity correlations observed for polarimeter events where the recoil proton falls within one of the large-angle scintillator slabs, beyond the acceptance of the tracking detectors. The azimuthal angle reconstructed for the forward proton is plotted vs. the vertical position inferred for the recoil proton from the time difference δt between the top and bottom phototubes on the large-angle slab.

During multi-particle trigger running, we normally devoted 10–20% of the beam spills to collecting data with a polarimeter trigger (see Section 4.1), designed to select events satisfying the correlation of left and right hodoscope elements expected for the four elastic scattering groups of interest: 1 = forward proton on the left arm near 14° laboratory angle; 2 = forward proton on the right arm near 14°; 3 = forward proton on the left arm near 24°; 4 = forward proton on the right arm near 24°. When the analyzed events from these beam spills satisfy the additional software elastic scattering conditions described above, they are sorted into a histogram of polarimeter group yield vs. beam spin direction. The asymmetry $\varepsilon = A_y P_{\text{beam}}$ can then be independently determined from groups 1 and 2 or groups 3 and 4. For example, the average of spin-up and spin-down polarizations is deduced from

$$\varepsilon = \frac{r-1}{r+1}$$

with

$$r = (r_{\text{L}}/r_{\text{R}})^{1/2},$$

$$r_{\text{L}} = \frac{Y_{1(3)\uparrow}}{Y_{1(3)\downarrow}}, \qquad r_{\text{R}} = \frac{Y_{2(4)\uparrow}}{Y_{2(4)\downarrow}},$$

where Y represents the deadtime-corrected elastic scattering yield, normalized against the integrated beam for the given beam spin orientation (designated by the arrow subscript), and the numerical subscripts refer to the polarimeter group (hence, to the side of the beam on which the forward proton is detected). Typical values of ε for 2.85 GeV bombarding energy are: $\varepsilon(\text{groups } 1, 2) = 0.110$; $\varepsilon(\text{groups } 3, 4) = 0.130$. Introducing the available data [11] for A_y, one gets an average beam polarisation of $\approx 73\%$ for all the measurements performed at a beam energy of 2.85 GeV.

Instrumental asymmetries have been checked by evaluating the asymmetries based on r_{L} and on r_{R} alone, in addition to the cross-ratio method outlined above. As an example, the resulting asymmetries ε_{L} and ε_{R} are compared to ε as a function of run number in Fig. 17. The left and right systematic deviations from ε (which might arise, e.g., from correlations of beam position or beam integration errors with beam spin orientation) are within 5%. The instrumental asymmetry contributions to
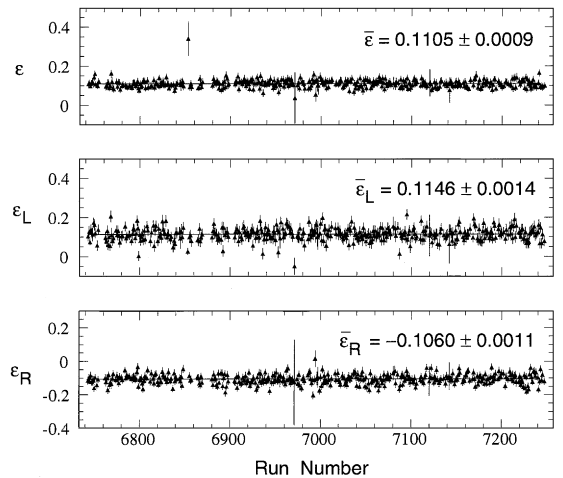

Fig. 17. Asymmetries for pp elastic scattering near 14° measured with the DISTO polarimeter at 2.85 GeV versus run number. See text for definitions of asymmetries. Upper frame ε, medium frame ε_{L} and lower frame ε_{R}.

ε should be smaller than this by at least an additional order of magnitude. It is clear from Fig. 17 that the beam polarization was remarkably stable during the data taking.

6. Conclusion

The DISTO apparatus was fully commissioned at Saturne in summer 1996. It was used extensively in production runs until the Saturne shutdown in December 1997, for studying, at the same time, two-body and many-body reactions with beams of polarized protons. The beam energies ranged from 1.6 to 2.85 GeV. Trigger rates as large as 3000 per spill, corresponding to $\approx$ 1 Mbyte of information collected in 0.4 s, were handled with $\approx$ 10% deadtime. A momentum resolution $\sigma \approx 5\%$ has been obtained for particle momenta between 1.5 and 2.5 GeV/c. At the vertex reconstructed from p and π^- tracks, the Λ invariant mass peak is reconstructed with a resolution $\sigma \simeq 5$ MeV/c^2. When four tracks are reconstructed, as in the pp $\rightarrow$ pK$^+\Lambda$ or pp $\rightarrow$ ppK$^+$K$^-$ reactions, resolutions in the missing mass spectra $\sigma \lesssim 30$ MeV/c^2 have been reached in the analysis to date, and further improvements are expected. Kaon particle identification was sufficiently clean to suppress $\pi^+\pi^-$ background by nearly three orders of magnitude, as needed to reveal a clear signal for the weak ϕ production channel. In the case of the pp $\rightarrow$ pK$^+\Lambda$ reaction, a sample $\sim 10^5$ events was acquired at each of three bombarding energies, to allow determination of analyzing powers, outgoing Λ polarizations, and polarization transfer coefficients for the reaction.

The results obtained will provide a wealth of new information to constrain the mechanism for various exclusive nucleon–nucleon reaction channels, especially those involving the production of open or hidden strangeness.

Acknowledgements

References

[1] R. Bertini, in: B. Frois, D. Goutte, P.J. Mulders, P.K.A. De Witt Huberts (Eds.), Proc. 1st European Workshop on Hadronic Physics in the 1990's with Multi-GeV Electrons, Seillac, France, June 27–July 1, 1989; Nucl. Phys. A 497 (1989) 307c.

[2] K. Heller, in: A. Boudard, Y. Terrien (Eds.), Proc. Int. Conf. on Polarization Phenomena in Nuclear Physics, Paris, July 9–13, 1990; Colloque Phys. 51 (1990) C6–163, and references therein.

[3] G. Bardin et al., Nucl. Instr. and Meth. A 259 (1987) 376.

[4] P.F. Dalpiaz, private communication.

[5] P. Senger et al., Nucl. Instr. and Meth. A 327 (1993) 393.

[6] F. Balestra et al., IEEE Trans. Nucl. Sci. NS-45 (1998) 817.

[7] F. Balestra et al., IEEE Trans. Nucl. Sci. NS-45 (1998) 868.

[8] R. Brun et al., PAW User's Guide, CERN Program Library Q121.

[9] R. Brun et al., GEANT User's Guide, CERN Program Library W5103.

[10] H. Wind, Nucl. Instr. and Meth. 115 (1974) 431.

[11] F. Lehar, in: A. Boudard, Y. Terrien (Eds.), Proc. Int. Conf. on Polarization Phenomena in Nuclear Physics, Paris, July 9–13, 1990, Colloque Phys. 51 (1990) C6-19, and references therein

[12] Ch. Allgower et al., Laboratoire National Saturne internal Report LNS/Ph/97-11, 1997.